Particulate Science and Technology, 32: 224–233

ISSN: 0272-6351 print/1548-0046 online
DOI: 10.1080/02726351.2013.850460

Taylor & Francis
Taylor & Francis Group

Water-Soluble Anisotropic Iron Oxide Nanoparticles: Dextran-Coated Crystalline Nanoplates and Nanoflowers

SOUBANTIKA PALCHOUDHURY,[1] FAHMEED HYDER,[2] T. KYLE VANDERLICK,[1] and NIENKE GEERTS[1]

[1]*Department of Chemical and Environmental Engineering, Yale University, New Haven, Connecticut, USA*
[2]*Department of Biomedical Engineering and Diagnostic Radiology, Yale University, New Haven, Connecticut, USA*

We report a simple phase transfer based synthesis route for two novel anisotropic water soluble iron oxide nanoparticle shapes, namely, nanoplates and nanoflowers. The nanoplates and nanoflowers are initially prepared in an organic solvent via a modified ''heat-up'' method. Then, the crystalline nanoparticles are rendered hydrophilic via sonication in the presence of dextran and water. These nanoparticles are highly monodisperse and superparamagnetic at room temperature. High resolution transmission electron microscopy indicates that the iron oxides cores are not affected by the phase transfer. Dextran coating is confirmed by dynamic light scattering, Fourier transform infrared spectroscopy, and thermogravimetric analysis. The obtained dextran coverage was 26 wt% for the nanoplates and 37 wt% for the nanoflowers. The nanoplates and nanoflowers were not only water soluble, but also remained stable at different pH (4–7) and in common aqueous buffer solutions. Thorough characterizations of the nonspherical iron oxide nanoparticles indicate that these particles could be useful for potential biomedical applications and magnetic resonance imaging.

Keywords: Materials, nanoparticles, nonspherical particle, particle characteristics, particle shape

1. Introduction

Iron oxide nanoparticles (NPs) have been extensively studied for biomedical applications, such as targeted drug delivery, localized cancer therapy, and as contrast agents for magnetic resonance imaging (MRI) (Sonvico et al. 2005; Sun et al. 2008; Laurent et al. 2008; Fang and Zhang 2009; Yiu et al. 2013). These extensive studies led to the realization of clinically approved magnetic iron oxide particles, such as Ferridex and Ferucarbotran. Although these particles are currently extensively used, their shape and preparation method present two limitations. First, the mentioned studies focus on spherical NPs, primarily because the synthesis of anisotropic iron oxide NPs is more challenging. Second, due to their preparation method, the materials are often of low crystallinity.

Compared to nanospheres, nonspherical iron oxide NPs have shown promising advantages in biomedical applications. Nonspherical NPs could be preferred because of their shape-dependent applications in sensing and catalysis (Jun et al. 2006). Anisotropic worm-like shaped particles exhibited prolonged blood circulation times (Park et al. 2008), and nonspherical NPs showed increased intercellular adhesion and retention in tumors (Tao et al. 2008). Therefore, an emerging strategy is to control the shape-dependent properties of iron oxide NPs for biological applications. Although the above mentioned anisotropic NPs show great promise, their preparation method (co-precipitation) poses the second limitation.

Particles produced by a co-precipitation method results into iron oxide NPs with a wide size distribution and low crystallinity. As these parameters directly influence the magnetic properties of these NPs, it limits their performances as magnetic resonance imaging (MRI) contrast agents. High quality iron oxide NPs regarding monodispersity, size distribution, and crystallinity can currently only be produced in organic solvents at high temperatures. This so called ''heat-up'' method generates iron oxide NPs with a great amount of control over particle size, composition, and shape (Park et al. 2004). A well-controlled synthesis of iron oxide nanoplates and nanoflowers in organic solvent was recently reported. These novel NPs could be potentially useful in exploring the shape-dependent bio-applications (Palchoudhury et al. 2012). For biological applications, surface modification to achieve water soluble NPs is essential. Typically, the NPs can be transferred from organic solvents to aqueous solutions through attachment of amphiphilic ligands (Gonzales and Krishnan 2007; Prakash et al. 2009; Yu et al. 2006) or replacement of the hydrophobic coatings by hydrophilic molecules (Xu et al. 2011; Binder et al. 2008).

Here, we report the transfer of crystalline iron oxide nanoplates and nanoflowers into the aqueous phase with the use of dextran. Although the reproducible synthesis of

Address correspondence to: Nienke Geerts, Department of Chemical and Environmental Engineering, Yale University, New Haven, CT 06511, USA. E-mail: nienke.geerts@yale.edu
Color versions of one or more of the figures in the article can be found online at www.tandfonline.com/upst.

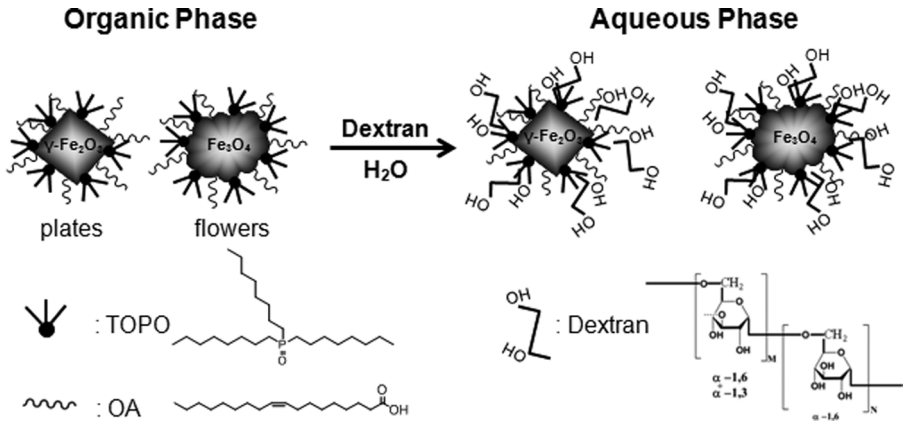

Fig. 1. Schematic illustration of the addition of dextran to make the iron-oxide particles water soluble. A full ligand exchange was not attempted as this will affect the shape of the particles.

these anisotropic iron oxide particles has been reported before (Palchoudhury et al. 2012), this is to our knowledge the first attempt at rendering the NPs hydrophilic using a dextran based bilayer phase transfer (Figure 1). The phase transfer through attachment of amphiphilic ligands is not a trivial execution as this often results in multiple NPs being collectively coated within an envelope of the capping molecule (Euliss et al. 2003). Full ligand replacement is in this case not desirable, while the organic ligands are partially responsible for the anisotropic shapes. Dextran was selected as it is readily available, inexpensive, and approved as a coating for NPs in clinical studies by the Food & Drug Administration (FDA) (Reimer and Balzer 2003).

To confirm the surface attachment of dextran, the iron oxide nanoplates and nanoflowers are extensively characterized. Transmission electron microscopy (TEM) is used to confirm the shape and size of the NPs. With two dimensional power x-ray diffraction (XRD2) the crystallinity of the NPs is further confirmed. The hydrodynamic dimensions of the aqueous nanoplate and nanoflower dispersions were measured with dynamic light scattering (DLS). Fourier transform infrared spectroscopy (FTIR) is used to show the change in outer surface ligands after the phase transfer from organic solvents to aqueous solutions, while thermogravimetric analysis (TGA) was used to examine the complete coating. Moreover, magnetic measurements confirmed the superparamagnetic nature of the water soluble particles. Additionally, the stability of the dextran-coated nanoplates and nanoflowers was characterized over a 28 day period at different pH and for three commonly used buffer solutions (phosphate buffered saline (PBS), saline sodium citrate (SSC), and 4-(2-hydroxyethyl)-1-piperazineethanesulfonic acid (HEPES)).

In summary, this study provides a phase transfer based facile route for the formation of crystalline dextran-coated iron oxide NPs of two different anisotropic shapes. These results will be useful for the growing application of nonspherical NPs in biomedical fields (Geng et al. 2007; Zhao et al. 2013) and potentially even for blood volume imaging with MRI where dextran-coated iron oxide NPs have high specificity for the plasma compartment (Herman et al. 2009).

2. Materials and Methods

2.1 Materials

Reagents were used as purchased, including: iron (III) chloride (anhydrous, 98%, Alfa Aesar, Ward Hill, MA, USA), sodium oleate (Spectrum), 1-octadecene (90%, Acros, Bridgewater, MA, USA), tri-*n*-octylphosphine oxide (TOPO, 90%, Sigma-Aldrich), oleic acid (OA, 90%, Alfa Aesar), dextran (high fraction, $M_W = 250\ 000$, Acros), chloroform ($\geq$99.8%, Sigma Aldrich, St. Louis, MO, USA), acetone ($\geq$99.5%, Sigma Aldrich), *n*-hexane (Sigma Aldrich), ethyl alcohol (Pharmco Aaper, Brookfield, CT, USA), 4-(2-hydroxyethyl)-1-piperazineethanesulfonic acid (HEPES, $\geq$99.5%, Sigma), saline sodium citrate (SSC, Life Technologies, Grand Island, NY, USA), and phosphate buffered saline (PBS, Sigma).

2.2 Synthesis of the Iron Oxide Nanoplates and Nanoflowers

Iron oxide nanoplates and nanoflowers were prepared from the thermal decomposition of an iron oleate complex, following a similar procedure reported earlier (Palchoudhury et al. 2012) The iron oleate precursor was prepared as follows: sodium oleate (36.5 g) and ferric chloride (6.5 g) were mixed in a solvent mixture (hexane, 140 mL; ethanol, 80 mL; de-ionized water, DI, 60 mL) at 60°C. After phase separation, the organic phase containing iron oleate complex was washed three times with deionized (DI) water to remove by-products such as KCl. The resulting product, an iron oleate complex with 6 wt% hexane, served as the precursor for subsequent nanoplate and nanoflower synthesis.

To obtain nanoplates and nanoflowers the iron oleate hexane precursor solution (1.82 g) was heated at 290°C for 1 h in 1-octadecene (13 mL) in the presence of two additional ligands, OA (0.1 mL) and TOPO (0.2 g nanoplates and 1 g nanoflowers). The crystalline products were precipitated out of the solution with an acetone/chloroform mixture, magnetically separated to wash off 1-octadecene and unreacted organics, and vacuum dried overnight. The well dried powders of nanoplates and nanoflowers were redispersed in hexane via sonication to obtain stock solutions of 50 mg/mL.

2.3 Calculation for the Quantity of Dextran Required for Effective Phase Transfer

The molar ratio of dextran to Fe atoms on nanoparticle (NP) surface was targeted at 5:1. The fraction of surface iron atoms was computed from the total number of atoms per particle as follows. Nanoplates and nanoflowers in 1 mL of the respective stock solutions (50 mg/mL) were well dried for the phase transfer procedure. First, the number of nanoplates and nanoflowers were calculated via dividing the weight used (50 mg) by the mass of a single NP ($4/3\pi r^3\rho$). Here, ρ is the density of bulk iron oxide (γ-Fe_2O_3, 5.24 g/cm^3 for nanoplates and Fe_3O_4, 5.18 g/cm^3 for nanoflowers) and r is the longest radius of the NPs estimated from transmission electron microscopy (TEM) images. To estimate the moles of nanoplates and nanoflowers used, the resultant number was divided by the Avogadro's constant ($N_A = 6.023 \times 10^{23}$). Second, the cubic reactant on the nanoplate and nanoflower surface was computed using the formula, $4/3\pi r^3$ (i.e., NP volume)/volume of cubic unit cell (cell parameter 8.5 Å). Third, the fraction of unit cells on the nanoplate and nanoflower surface was estimated to 18%. Each of these unit cells was assumed to contribute a surface Fe atom. Therefore, the number of iron atoms on the nanoplate and nanoflower surface was obtained by multiplying the moles of NP with the surface cubic reactant and the surface unit cells. The moles of dextran used for phase transfer was set at 5 times the calculated number of Fe atoms on the NP surfaces.

2.4 Phase Transfer of the Nanoplates and Nanoflowers

The nanoplate or nanoflower stock solution (1 mL) was mixed with dextran (M_W 250 000) such that the molar ratio of biocompatible ligand-to-NP surface Fe atoms was approximately set to 5:1 (Park et al. 2004). After sonication (5 min), slight mixing was observed in this solution. Ultra-pure water (5 mL, Millipore) was added to the nanoplate-dextran solution forming two phase separated layers. To transfer the plates or flowers to the aqueous phase, the solution was vortexed (Vortex genie 2; Scientific Industries, room temperature (RT)) and sonicated (Branson 5510 sonicator; Fisher Scientific, Waltham, MA, USA, RT) for 30 min. The homogeneous solution was left to phase separate overnight. Next, the aqueous dispersion of dextran-iron oxide nanoplates was collected with a syringe from the aqueous phase. The nanoplates were magnetically separated, weighed, and redispersed in water, prior to filtration through a syringe filter (pore size 0.2 μm, Whatman, Pittsburgh, PA, USA). The concentration of the nanoplates in the final aqueous dispersion was estimated to be 5 mg/mL. The water soluble particles were stable at RT for months without notable precipitation.

2.5 Characterization

The size and morphology of the iron oxide nanoplates and nanoflowers were investigated on a FEI Tecnai Osiris transmission electron microscope (TEM) using a double tilt holder. The nanoplates and nanoflowers in organic phase were centrifuged (1500 rpm, 15 min RT, Eppendorf MiniSpin) out with 1:1 ethanol/hexane (by volume), redispersed in hexane, and dropped on TEM grids for viewing. The aqueous phase samples were imaged without further treatment. Size histograms were obtained by measuring and plotting the size of 100 NPs. The hydrodynamic diameter and zeta potential of the nanoplates and nanoflowers were measured on a Malvern, Zetasizer nano DLS. The crystal structure of the dextran coated nanoplates and nanoflowers were examined with 2D powder diffraction (XRD2) using a Cu source (Rigaku; MicroMax-007HF generator and Saturn 944+ CCD detector; using 2θ scans (20–80°) and $K_{\alpha 1}$, $\lambda = 1.5416$ Å). Magnetic properties of the hydrophobic and aqueous phase nanoplates and nanoflowers were determined on a superconducting quantum interference device (SQUID) magnetometer at RT.

The surface attachment of dextran on the nanoplates and nanoflowers was evaluated with a Nicolet 6700 (Thermo Scientific) Fourier transform infrared spectrophotometer (FTIR), and thermogravimetric analyzer (TGA Q1000, TA Instruments). Powdered samples for XRD2, SQUID, TGA, and FTIR were prepared via centrifugation and overnight vacuum drying.

2.6 Stability Tests

The pH-dependent tests were conducted by carefully adjusting the nanoplate and nanoflower suspensions in water (pH 7, 1 mL) to the target values (pH 4, 5, 6, and 8) with HCl or NaOH, keeping all other parameters the same. The adjusted NP dispersions were sonicated (Branson 5510; Fisher Scientific) and left undisturbed till no change in pH was observed. The hydrodynamic diameter and zeta potential of these nanoplates and nanoflowers at different pH were measured over time (0, 7, 14, 21, and 28 days) using DLS.

The stability study was followed by examining the hydrodynamic diameter of nanoplates and nanoflowers in three common buffers (PBS, SSC, and HEPES). HEPES powder was dissolved in ultra-pure water via hand-shaking to achieve target aqueous buffer concentrations (0.1, 0.2, 0.5, 0.8, and 1 M). PBS (10 X; 80 g NaCl, 2 g KCl, 14.4 g Na_2HPO_4, and 2.4 g KH_2PO_4 in 950 ml H_2O) and SSC (10 X; 1.5 M NaCl and 0.15 M sodium citrate) were used as purchased. These buffers were diluted with ultra-pure water to obtain the targeted concentrations (1, 2, 5, 8, and 10 X). Final volumes of the HEPES, PBS, and SSC buffers of different concentrations were kept the same (5 mL). The NPs were added at target buffer concentrations (0.1, 0.2, 0.5, 0.8, and 1 M). Aqueous dispersions of the NPs (5 mL) were added to each buffer solution, prior to mixing by sonication (Branson 5510; Fisher Scientific). Well mixed nanoplate and nanoflower suspensions in the three buffers were measured for their hydrodynamic diameter and zeta potential with DLS.

3. Results

This work presents the phase transfer of two hydrophobic anisotropic iron oxide NPs, into the aqueous phase by attachment of dextran to the outer ligand surface. The exchange process is illustrated in Figure 1, where dextran

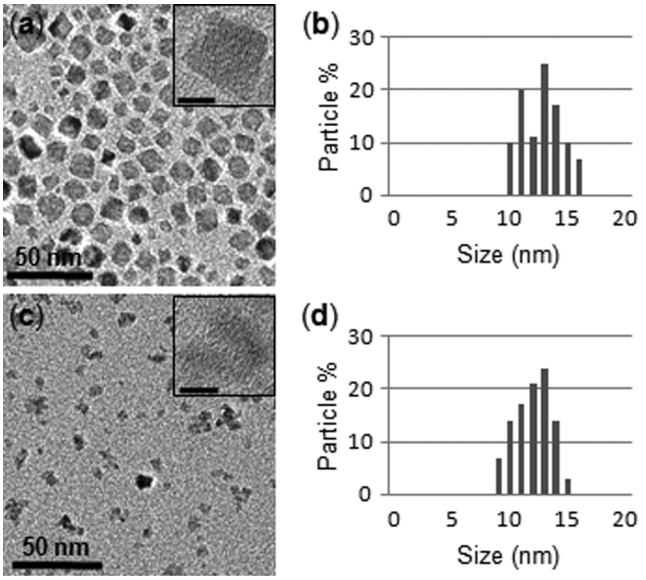

Fig. 2. TEM images of iron oxide nanoparticles in the organic phase: a) nanoplates, the insert is provided to show particles crystallinity; b) size distribution histogram of the nanoplates in the organic phase; c) nanoflowers, the insert is provided to show particles crystallinity; d) size distribution histogram of the nanoflowers in the organic phase. Scale bars 50 nm, insert scale bars 5 nm.

is added in addition to the two original coatings of the hydrophobic iron oxide NPs (oleic acid: OA) [Huang et al. 2013; Park et al. 2004] and trioctylphosphine oxide: TOPO [Palchoudhury et al. 2010]). The iron oxide nanoplates and nanoflowers are synthesized in an organic solvent in the presence of these two ligands as OA provides a compact binding to the NP surfaces to prevent inter-particle aggregation (Park et al. 2004), while TOPO, the weaker binding ligand, facilitates shape control (Palchoudhury et al. 2012).

Transmission electron microscopy (TEM) confirmed the formation of the two anisotropic shapes in the organic phase. Figure 2a shows a TEM image of monodispersed nanoplates. The nanoplates are crystalline (γ-Fe_2O_3) as shown by the lattice fringes in the high resolution transmission electron microscope (HRTEM) insert and $\sim 12 \times 14$ nm in size (Figure 2b). The iron oxide nanoflowers were formed from the coalescence of small nanocrystals (Figure 2c). The longest dimension of the nanoflowers is $\sim$14 nm (Figure 2d). The visible lattice fringes in the HRTEM insert proves the crystallinity (Fe_3O_4) for these particles as well. The hydrodynamic size of NPs was determined by DLS: OA- and TOPO-coated plates were 30 nm, the flowers 60 nm in diameter. The increase in size compared to the TEM is due to the fact that the TEM size histograms only reflect the iron oxide core, not the ligand coating.

To bring the as-synthesized hydrophobic anisotropic NPs into aqueous solution, a subsequent ligand attachment process was preceded by mixing the NP solution (50 mg/ml; the mass concentration includes both the iron oxide core and the organic coatings) with dextran in hexane. The relative ratio of the NP-to-ligand was calculated to ensure the ratio of the surface iron atoms to ligands were roughly 1 to 5. (A previous determined optimum (Xu et al. 2011), see Materials and Methods for detailed explanation of the calculation.) After addition of water (pH 7) and 30 min of sonication the homogeneous solution was left to phase separate overnight. The nanoplates were magnetically separated, weighed, and redispersed in water. The efficacy of the ligand exchange process was confirmed by FTIR, TGA, the hydrodynamic sizes, and the zeta potentials of the resultant NPs.

Figure 3 shows the TEM images of the nanoplates (a) and nanoflowers (d) in the aqueous phase. Compared with the as-synthesized NPs (Figure 2) the uniformity, morphology,

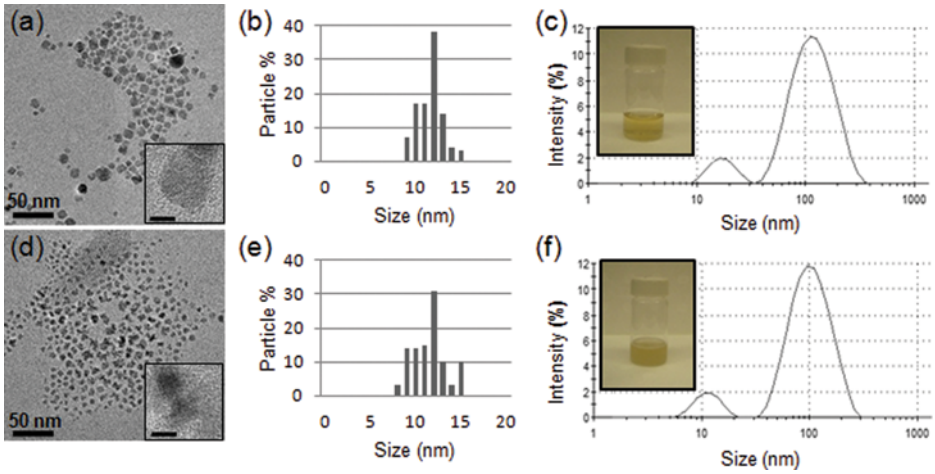

Fig. 3. Iron oxide nanoparticles in the aqueous phase. a) TEM image of nanoplates, the insert is provided to show particles crystallinity; b) size distribution histogram of the nanoplates in the aqueous phase; c) average size of the nanoplates as determined by DLS (the insert picture is to show plates stability in water); d) TEM image of nanoflowers, the insert is provided to show particles crystallinity (scale bars 50 nm, insert scale bars 5 nm); e) size distribution histogram of the nanoflowers in the aqueous phase; f) average size of the nanoflowers as determined by DLS. (the insert picture is to show flowers stability in water).

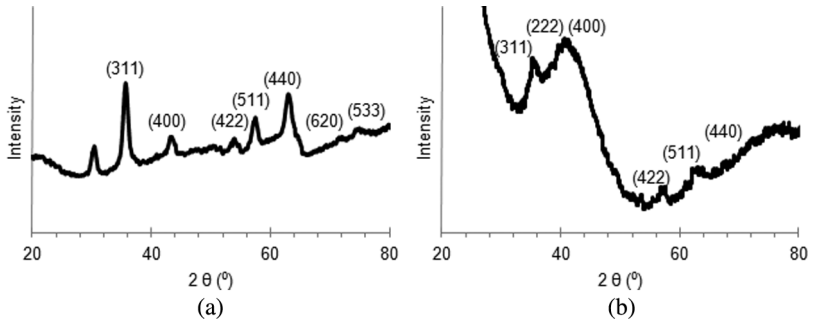

Fig. 4. Two-dimensional powder diffraction scans: a) dextran-coated nanoplates; maghetite (γ-Fe_2O_3); b) dextran-coated nanoflowers; magnemite (Fe_3O_4).

and core size (Figures 3b and 3e) did not show evident changes. Both the nanoplates and the nanoflowers remain in solution over prolonged periods of time, without any noticeable precipitation (Figures 3c and 3f inserts). The hydrodynamic sizes of the dextran coated NPs are about 80 nm for the plates and 76 nm for the flowers. The size increase for both particle types is indicative for the additional dextran coating.

The XRD2 scans of dextran-coated nanoplates and nanoflowers (Figure 4) show typical iron oxide peaks, suggesting good crystallinity. The size broadening of the diffraction peaks is owed to the nanometer sizes of the crystallites. The 2θ peaks of the hydrophilic nanoplates at 30°, 35.4°, 42.7°, 53°, 57°, 62.6°, 71°, and 75.5° (Cu source, $K_{\alpha 1}$ $\lambda = 1.5416$ Å) correspond well to (220), (311), (400), (422), (511), (440), (620), and (533) expected crystal planes of γ-Fe_2O_3 (Figure 4a). Particularly, the presence of the (620) and (533) peaks of comparable intensity distinguish the maghemite phase of the nanoplates from the more common magnetite phase (Liu et al. 2003). The iron oxide nanoplates were already characterized to be of maghemite crystal phase in an earlier report (Palchoudhury et al. 2012), here we show that addition of a dextran coating does not affect this. Figure 4b shows the XRD2 scan of dextran-coated nanoflowers. A completely dry powdered sample of the dextran-nanoflowers was difficult to prepare, likely due to the heavy ligand coverage. Therefore, the nanoflowers show less prominent peaks compared to the nanoplates. For the nanoflowers, the 2θ peaks found at 35.05°, 38.08°, 41°, 52.5°, 56.5°, and 62° match well with the (311), (222), (400), (422), (511), and (440) crystal planes of magnetite. Especially, the presence of a (222) peak and comparable intensities of the (311) and (400) peak are indicative of a magnetite (Fe_3O_4) crystal phase (Liu et al. 2003; Palchoudhury et al. 2012). Hence, the iron oxide core of the nanoflowers is also preserved after the addition of a dextran coating.

The FTIR spectra (Figures 5a and 5b) of the hydrophilic NPs further confirmed the attachment of dextran. Compared to the spectra of the as-synthesized NPs, the hydrophilic nanoplates and flowers have distinctive OH peaks at $\sim$3300 cm^{-1}, and water molecule bending at $\sim$1640 cm^{-1}, characteristic of dextran binding. The slight shift in this OH peak compared to pure dextran suggests adsorption to the surface. Additionally, the bands around 1010 cm^{-1} can be assigned to the alcoholic C-O stretch from the carbon attached to OH in dextran. Furthermore, typical peaks for as-synthesized particles, like the saturated C-H stretch (Sherman Hsu 1997) around 2900 and 2840 cm^{-1}, the P=O presence (Young et al. 2008) of TOPO around 980 and surface conjugated carboxyl groups (Fang et al. 2009; Bronstein et al. 2007) of OA, indicated by the peaks at 1564 and

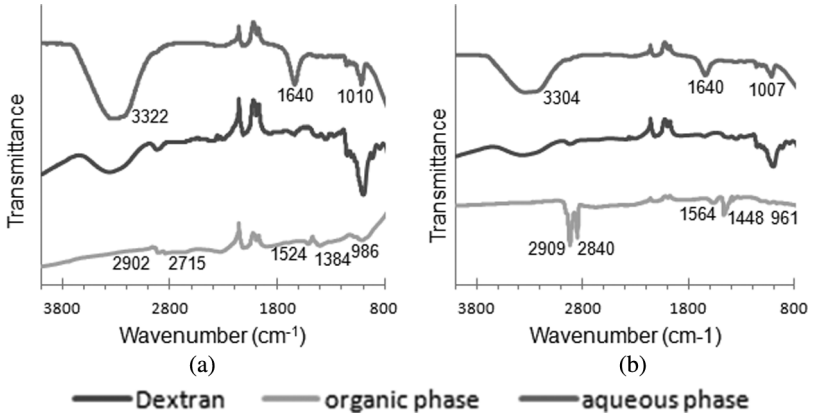

Fig. 5. a) FTIR spectra of iron oxide nanoplates in the organic and aqueous phase b) FTIR spectra of iron oxide nanoflowers in the organic and aqueous phase. For comparison a FTIR spectra of dextran is added to both graphs.

1448 cm^{-1}, were absent in the spectra of the dextran-coated NPs. Another important observation is the absence of typical peaks for covalent dextran iron oxide bonds around 900–800 cm^{-1} (Jung 1995), indicating that the dextran indeed formed an outer bilayer instead of binding covalently to the nanoplate and nanoflower surfaces. For clarity the spectrum of dextran is added to both graphs. Compared to pure dextran, the dextran-nanoplates and nanoflowers show a stronger band at 1640 cm^{-1}, presumably due to adsorbed water during processing.

To further investigate the composition of the iron oxide nanoplates and nanoflowers, the surfactants were thermally removed (TGA) to determine the weight percentages of all ligands attached to the NPs (TOPO/OA/dextran). Figure 6a shows the TGA plot for the hydrophobic nanoplate powder samples. Three distinct weight loss peaks at 260°C, 480°C, and 740°C were observed through controlled heating of the sample (10°C/min) up to 800°C under N_2 atmosphere. The initial weight loss up to 100°C is not indicative of one of the ligands, rather this peak is due to desorption of chloroform and/or acetone that physically adsorbed in the washing steps. The weight loss around 260°C can be assigned to the removal of TOPO from the nanoplate surfaces. TOPO is expected to be the first ligand for desorption as it shows a weaker and less compact binding to iron oxide NPs than OA does (Bao et al. 2010; Palchoudhury et al. 2010). The mass loss between 400 and 500°C corresponds to desorption of the outer layer of OA. As expected, it occurs at a temperature slightly higher than the boiling point of neat oleic acid or 360°C at 760 mm Hg (Morales et al. 2005). The third mass loss occurring around 650 and 800°C arises from desorption of the more tightly bound OA molecules. This inner layer of oleic acid is thought to be stabilized via a complex between iron and the carboxylate groups of oleic acid. As a result, it can only be removed from the surface at higher temperatures (Prakash et al. 2009). The TGA indicates that the organic surfactants covered ~29% (by weight) of the iron oxide nanoplates (Table 1).

In contrast to the hydrophobic particles, the dextran coated nanoplates showed a distinct peak not present in Figure 6a: ~26% weight loss around 300°C (Figure 6b). This peak indicates the thermal removal of the dextran coating (Tang et al. 2006). The peaks around 406°C (8 wt%) and 698°C (~20 wt%) represent the decomposition of bound organic surfactants. These additional peaks indicate that dextran is not fully replacing the OA and TOPO ligands. The initial weight loss around 122°C is assigned to the removal of physically adsorbed water. The plot reveals ~54 wt% total ligand coverage for the dextran-nanoplates (Table 1).

The hydrophobic nanoflowers showed heavier surfactant coverage (~87% by weight) than the nanoplates (Figure 6c). The two peaks at 457°C and 567°C are related to desorption of strongly bound organic surfactants (OA and TOPO; Hou et al. 2003; Mohapatra et al. 2013). However, the 87 wt% may be a small overestimate as the decomposition of the edge of the iron oxide core could also occur at these temperatures (Taylor et al. 2012). Compared to the organic phase nanoflowers, the hydrophilic nanoflowers exhibit an additional peak at 301°C. This peak corresponds to desorption of the dextran coverage (37 wt%; Figure 6d). The

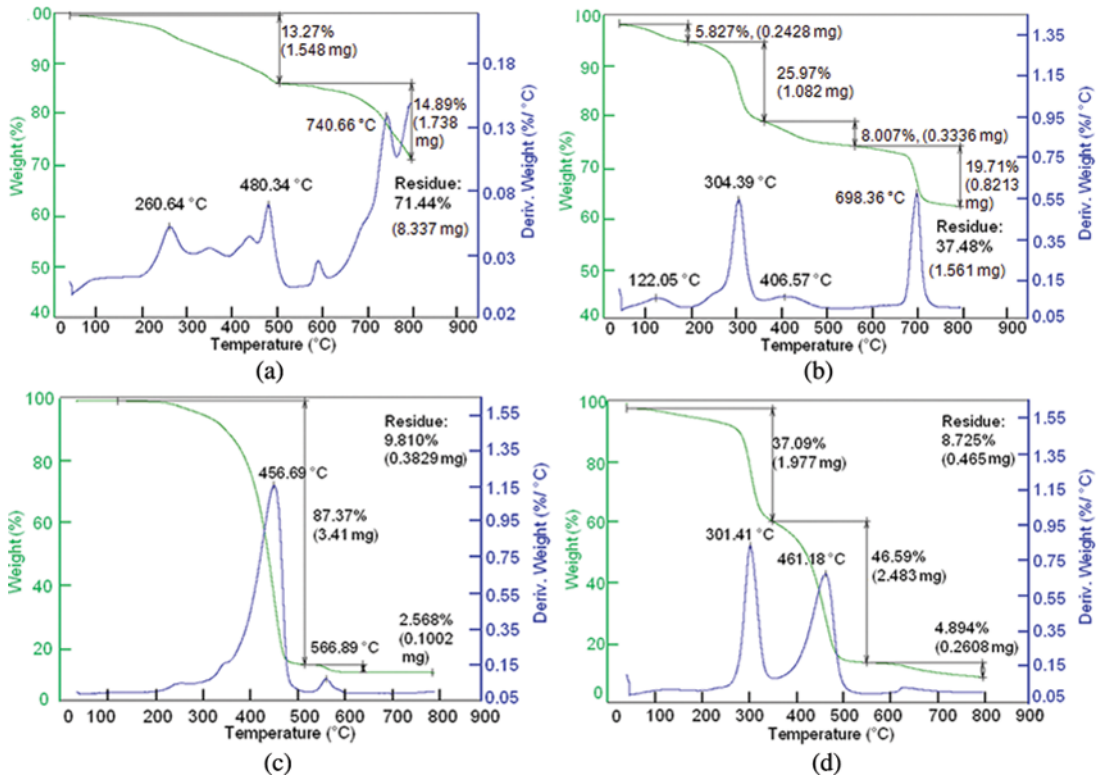

Fig. 6. TGA of the NPs a) plates organic, b) plates-dextran, c) flowers organic, and d) flowers dextran.

Table 1. Ligand coverage of the iron oxide nanoplates and nanoflowers

Sample	Ligand coverage (∼wt%)		
	Organic ligands	Dextran	Total
Hydrophobic nanoplates	29	X	29
Hydrophilic nanoplates	28	26	54
Hydrophobic nanoflowers	90	X	90
Hydrophobic nanoflowers	47	37	84

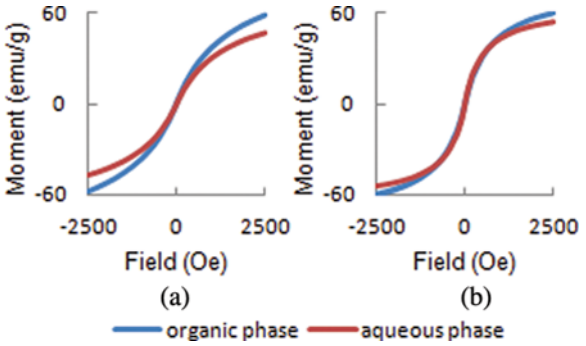

Fig. 7. Magnetic measurement of iron oxide nanoparticles; a) nanoflowers; b) nanoplates.

additional peak at 461°C accounts for the loss of remaining organic ligands (OA and TOPO). Once again the TGA confirms that the dextran coating is added on top of the organic ligands. The small mass loss (∼5%) above 570°C is from the transformation of Fe_3O_4 to FeO, the thermally stable phase at that elevated temperature (Zhao et al. 2006). The total surfactant coverage for the dextran-nanoflowers was approximately 84% (Table 1). The heavy dextran coverage for the nanoplates and nanoflowers is a promising aspect of our synthesis method, as a thick dextran layer prevents interaction with plasma proteins and opsonization (Jung 1995). This prevention is highly desirable for potential imaging and therapeutic applications.

The zeta potential value of a NP solution is an indicator of its stability, where a colloidal system is generally stable if this value is >-30 mV or <30 mV, but stable solutions of dextran coated iron oxide NPs have been reported with an out of range negative zeta potential (∼−10 mV—Sonvico et al. 2005; Griffiths et al. 2011; ∼−2 mV—Karmali et al. 2012). The nanoplates have a zeta potential of −13 mV in water, the nanoflowers −9 mV. The low absolute values of the zeta potentials indicate a lack of strong electrostatic charges on the NP surfaces. Therefore, the aqueous nanoplates and nanoflowers are most likely stabilized via steric hindrance of the dextran outer coating (Amstad et al. 2011).

To assess their preliminary potential in bio-applications such as MRI contrast enhancement, the magnetic properties of the particles are characterized using superconducting quantum interference magnetometer (SQUID). The magnetizations (M) versus applied magnetic field (H) curves of iron oxide plates and flowers before and after dextran attachment are shown in Figure 7. For the nanoplates, the saturation magnetization decreased from 60 emu/g (as-synthesized plates) to 53 emu/g for the hydrophilic plates, but the particles remained purely superparamagnetic (Figure 7b). The iron oxide nanoflower samples displayed a combination of superparamagnetism and paramagnetism, characteristic of NPs with high surface ligand coverage (Figure 7a). Both the hydrophobic and dextran-coated nanoflowers showed similar *M-H* curves without saturation. The magnetization of the nanoflowers at the highest observed values decreased from 58 emu/g to 47 emu/g after aqueous phase transfer. The absence of any ferromagnetic loops in the M-H curve of the iron oxide nanoplates and nanoflowers samples confirms stability (negligible aggregation).

The physicochemical properties of NPs in solution are dynamic and can be altered by the environment. The defined properties in water (e.g., hydrodynamic size, zeta potential), do not necessarily predict their performance during applications. Therefore, the stability of aqueous NP dispersions at various pH and in different buffer solutions is critical for in vivo bio-applications. For example, endocytosis is a common pathway of cellular internalization of iron oxide NPs for targeted imaging and drug delivery. During this uptake, the NPs are subjected to pH changes from 6.2 in the early endosomes to 4.6–5 for the lysosomes (Scott and Gruenberg 2011).

We monitored the aqueous dispersions of nanoplates and nanoflowers under related pH conditions (pH 4, 5, 6, and 7) over a 28 day period to examine the aggregation behavior (Figure 8). The size of the nanoplates changed instantly

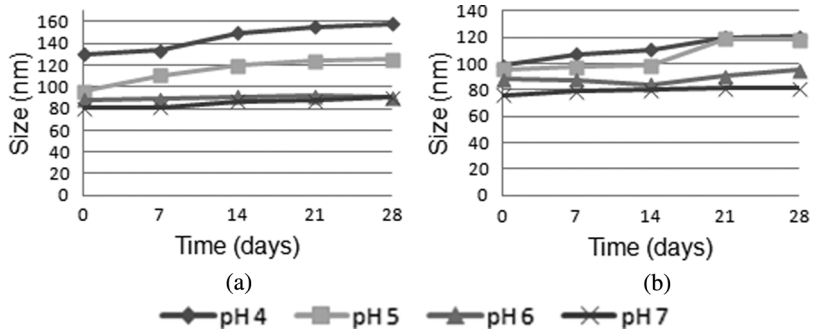

Fig. 8. Particle stability in water at different pH values; a) nanoplates; b) nanoflowers.

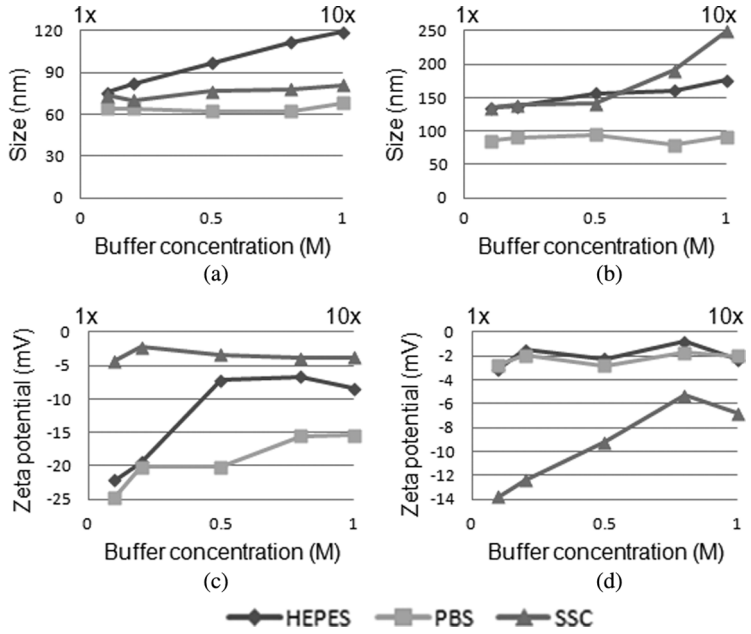

Fig. 9. Particle stability tested in three common buffers: a) nanoplates size (DLS); b) nanoflowers size (DLS); c) nanoplates zeta potential; d) nanoflowers zeta potential.

upon all pH changes, but stayed approximately the same with time for each pH tested (Figure 8a). This suggests good time-dependent stability, but also indicates that the pH changes do affect the dextran coating. For instance, at the lowest pH tested (pH 4), protonation of the hydroxyl groups of dextran takes place, strengthening the change of hydrogen bond formation between adjacent nanoplates, explaining the observed increase in size (Xu et al. 2011). Figure 8b shows the stability of the nanoflowers at different pH. The behavior is similar to the nanoplates, with smaller overall changes. Again, the slight increase in dimension at the more acidic values (pH 4 and 5) could be due to hydrogen bond formation. We would like to stress that no visible aggregation was observed for either shape and the hydrodynamic sizes remained well below 200 nm in all instances. This is promising for bio-applications because NPs of dimensions $<$200 nm can evade rapid clearance via macrophages.

The stability of NPs could also be affected by the ionic strength of a solution. While NPs eventually will be used under physiological conditions and not in pure water, their stability in common biology buffer is tested. Therefore the nanoplates and nanoflowers are monitored for their size and their zeta potential in HEPES (0.1–1 M), PBS (1–10 X), and SSC (1–10 X). The hydrodynamic size of the dextran-nanoplates is most stable in PBS (Figure 9a) with negligible variation from 63 nm to 68 nm. In SSC, the dextran coated nanoplates are stable as well. However, the nanoplates showed an appreciable size increase in HEPES (76–119 nm). The obtained zeta potentials are consistent with these findings. Values for dextran-nanoplates remained fairly constant for PBS (highly stable) and for SSC (stable), but displayed a significant increase (from -21 to -9 mV) for HEPES, suggesting instability (Figure 9c). Figure 9b shows the variation in hydrodynamic size of the dextran-nanoflowers with increasing ionic strength. Excellent stability was once again observed in PBS. The increase in hydrodynamic dimension (133–174 nm) suggests slight aggregation in HEPES. Different from the nanoplates, the dextran coated nanoflowers showed low stability in SSC, according to the significant change in size (135–248 nm). A possible explanation for this could be the different crystalline phase of the nanoflowers (Fe_3O_4 versus γ-Fe_2O_3 for the plates).

Aggregation was not visible in the TEM images of the dextran-nanoflowers at low buffer concentrations. Therefore, the aggregation behavior could be the result of salt bridge formation caused by the salt of the concentrated buffers. The zeta potentials of the nanoflowers confirmed well with the size measurements (Figure 9d) for the nanoflowers. For example, the zeta potentials of the nanoflowers were fairly constant in PBS and HEPES, but notably increased for SSC (-14 mV to -6 mV). The slight negative zeta potential of the nanoplates and nanoflowers is consistent with our hypothesis that the –OH groups of dextran protruded out in water to render the NPs hydrophilic. The $-$OH functionalities on the iron oxide nanoplates and nanoflowers could potentially provide active sites for bioconjugation (Pathak et al. 2001; Sperling and Parak 2010).

4. Conclusion

In summary, crystalline iron oxide nanoplates and nanoflowers with hydrophilic dextran coating were prepared. The anisotropic NPs were synthesized via the modified

"heat-up" method to obtain excellent shape and size control. A facile phase transfer route was explored to coat the organic NPs with an additional dextran layer. FTIR analyses indicated successful adsorption of a dextran bilayer on the nanoplate and nanoflower surfaces. The dextran-coated hydrophilic nanoplates and nanoflowers were most stable in aqueous dispersions of pH 6–7 for water and in PBS. Both the nanoplates and nanoflowers are sterically stabilized via dextran with the polyhydroxylated groups of dextran extending out to the solution phase, as suggested by the low absolute values of zeta potential. Detailed theoretical investigations and computer simulations on the dextran bilayer-NP binding interactions are being pursued. We believe the present work can be extended to other anisotropic NPs. The dextran based phase transfer for anisotropic NPs will offer promising applications in targeted imaging and therapy (Nidhin et al. 2013).

Acknowledgments

We acknowledge Yale Institute of Nanoscience and Quantum Engineering (YINQE) for TEM facilities. We thank Elias Quijano and Dr. Saltzman for use of the DLS. Thanks are due to Teng-hooi Goh and Dr. Andre Taylor for use of the TGA. We also acknowledge the Chemical and Biophysical Instrumentation and specifically Dr. Wuyi Meng at Yale for FTIR and XRD2 facilities.

References

Amstad, E., M. Textor, and E. Reimhult. 2011. Stabilization and functionalization of iron oxide nanoparticles for biomedical applications. *Nanoscale* 3:2819–2843.

Bao, Y., W. An, C. H. Turner, and K. M. Krishnan. 2010. The critical role of surfactants in the growth of cobalt nanoparticles. *Langmuir* 26:478–83.

Binder, W. H., H. Weinstabl, and R. Sachsenhofer. 2008. Superparamagnetic ironoxide nanoparticles via ligand exchange reactions: organic 1, 2-diols as versatile building blocks for surface engineering. *Journal of Nanomaterials* 383020(1–10).

Bronstein, L. M., X. Huang, J. Retrum, A. Schmucker, M. Pink, B. Stein, and B. Dragnea. 2007. Influence of iron oleate complex structure on iron oxide nanoparticle formation. *Chemistry of Materials* 19:3624–3632.

Euliss, L. E., S. G. Grancharov, S. O'Brien, T. J. Deming, G. D. Stucky, C. B. Murray, and G. A. Held. 2003. Cooperative assembly of magnetic nanoparticles and block copolypeptides in aqueous media. *Nano Letters* 3:1489–1493.

Fang, C., N. Bhattarai, C. Sun, and M. Zhang. 2009. Functionalized nanoparticles with long-term stability in biological media. *Small* 5:1637–1641.

Fang, C., and M. Zhang. 2009. Multifunctional magnetic nanoparticles for medical imaging applications. *Journal of Materials Chemistry* 19:6258–6266.

Geng, Y., P. Dalhaimer, S. Cai, R. Tsai, M. Tewari, T. Minko, and D. E. Discher. 2007. Shape effects of filaments versus spherical particles in flow and drug delivery. *Nature Nanotechnology* 2:249–255.

Gonzales, M., and K. M. Krishnan. 2007. Synthesis of magnetoliposomes with mondisperse iron oxide nanocrystals cores for hyperthermia. *Journal of Magnetism and Magnetic Materials* 311:59–62.

Griffiths, S. M., N. Singh, G. J. S. Jenkins, P. M. Williams, A. W. Orbaek, A. R. Barron, C. J. Wright, and S. H. Doak. 2001. Dextran coated ultrafine superparamagnetic iron oxide nanoparticles: compatibility with common fluorometric and colorimetric dyes. *Analytical Chemistry* 83:3778–3785.

Herman, P., B. G. Sanganahalli, and F. Hyder. 2009. Multi-modal measurements of blood plasma and red blood cell volumes during functional brain activation. *Journal of Cerebral Blood Flow & Metabolism* 29:19–24.

Huang, J., L. Wang, R. Lin, A. Y. Wang, L. Yang, M. Kuang, W. Qian, and H. Mao. 2013. Casein-coated iron oxide nanoparticles for high MRI contrast enhancement and efficient cell targeting. *ACS Applied Materials & Interfaces* 5:4632–4639.

Hou, Y., J. Yu, and S. Gao. 2003. Solvothermal reduction synthesis and characterization of superparamagnetic magnetite nanoparticles. *Journal of Materials Chemistry* 13:1983–1987.

Jun, Y. W., J. S. Choi, and J. Cheon. 2006. Shape control of semiconductor and metal oxide nanocrystals through nonhydrolytic colloidal routes. *Angewandte Chemie International Edition* 45:3414–3439.

Jung, C. W. 1995. Surface properties of superparamagnetic iron oxide MR contrast agents: ferumoxides, ferumoxtran, ferumoxsil. *Magnetic Resonance Imaging* 13:675–691.

Karmali, P. P., Y. Chao, J-H. Park, M. J. Sailor, E. Ruoslahti, S. C. Esener, and D. Simberg. 2012. Different effect of hydrogelation on antifouling and circulation properties of dextran-iron oxide nanoparticles. *Molecular Pharmacology* 9:539–545.

Laurent, S., D. Forge, M. Port, A. Roch, C. Robic, L. Vander Elst, and R. N. Muller. 2008. Magnetic iron oxide nanoparticles: synthesis, stabilization, vectorization, physicochemical characterizations, and biological applications. *Chemical Reviews* 108:2064–2110.

Liu, K., L. Zhao, P. Klavins, F. E. Osterloh, and H. Hiramatsu. 2003. Extrinsic magnetoresistance in magnetite nanoparticles. *Journal of Applied Physics* 93:7951–7954.

Mohapatra, J., A. Mitra, D. Bahadur, and M. Aslam. 2013. Surface controlled synthesis of MFe_2O_4 (M=Mn, Fe, Co, Ni and Zn) nanoparticles and their magnetic characteristics. *Cryst. Eng. Comm.* 15:524–532.

Morales, M. A., T. K. Jain, V. Labhasetwar, and D. L. Leslie-Pelecky. 2005. Magnetic studies of iron oxide nanoparticles coated with oleic acid and pluronic (R) block copolymer. *Journal of Applied Physics* 97:10Q905.

Nidhin, M., S. S. Nazeer, R. S. Jayasree, M. S. Kiran, B. U. Nair, and K. J. Sreeram. 2013. Flower shaped assembly of cobalt ferrite nanoparticles: application as T2 contrast agent in MRI. *RSC Advances* 3:6909–6912.

Palchoudhury, S., Y. Xu, W. An, C. H. Turner, and Y. Bao. 2010. Platinum attachments on iron oxide nanoparticle surfaces. *Journal of Applied Physics* 107:09B311.

Palchoudhury, S., Y. Xu, A. Rushdi, R. A. Holler, and Y. Bao. 2012. Controlled synthesis of iron oxide nanoplates and nanoflowers. *Chemical Communications.* 48:10499–10501.

Park, J., K. An, Y. Hwang, J. G. Park, H. J. Noh, J. Y. Kim, J. H. Park, N. M. Hwang, and T. Hyeon. 2004. Ultra-large-scale synthesis of monodispersed nanocrystals. *Nature Materials* 3:891–895.

Park, J. H., G. Von Maltzahn, L. Zhang, M. P. Schwartz, E. Ruoslahti, S. N. Bhatia, and M. J. Sailor. 2008. Magnetic iron oxide nanoworms for tumor targeting and imaging. *Advanced Materials* 20:1630–1635.

Pathak, S., S. K. Choi, N. Arnheim, and M. E. Thompson. 2001. Hydroxylated quantum dots as luminescent probes for in situ hybridization. *Journal of the American Chemical Society* 123:4103–4104.

Prakash, A., H. Zhu, C. J. Jones, D. N. Benoit, E. J. Ellsworth, B. N. Bryant, and V. L. Colvin. 2009. Bilayers as phase transfer agents for nanocrystals prepared in nonpolar solvents. *ACS Nano* 3:2139–2146.

Reimer, P., and T. Balzer. 2003. Ferucarbotran (resovist): A new clinically approved RES-specific contrast agent for contrast-enhanced MRI of the liver: properties clinical development, and applications. *European Radiology* 13:1266–1276.

Scott, C., and J. Gruenberg. 2011. Ion flux and the function of endosomes and lysosomes: pH is just the start. *Bioessays* 33:103–110.

Sherman Hsu, C. P. 1997. *Infrared spectroscopy*. In *Handbook of instrumental techniques for analytical chemistry*, (F. A. Settle, ed.), 247–283. Upper Saddle River, NJ: Prentice Hall.

Sonvico, F., S. Mornet, S. Vasseur, C. Dubernet, D. Jaillard, J. Degrouard, et al. 2005. Folate-conjugated iron oxide nanoparticles for solid tumor targeting as potential specific magnetic hyperthermia mediators: Synthesis, Physicochemical characterization, and in vitro experiments. *Bioconjugate Chemistry* 16:1181–1188.

Sperling, R. A., and W. J. Parak. 2010. Surface modification, functionalization and bioconjugation of colloidal inorganic nanoparticles. *Philosophical Transactions of the Royal Society A* 368:1333–1383.

Sun, C., J. S. H. Lee, and M. Zhang. 2008. Magnetic nanoparticles in MR imaging and drug delivery. *Advanced Drug Delivery Reviews* 60:1252–1265.

Tang, M., H. Dou, and K. Sun. 2006. One-step synthesis of dextran-based stable nanoparticles assisted by self-assembly. *Polymer* 47:728–734.

Tao, L., W. Hu, Y. Liu, G. Huang, B. D. Sumer, and J. Gao. 2011. Shape-specific polymeric nanomedicine: Emerging opportunities and challenges. *Experimental Biology and Medicine* 236:20–29.

Taylor, R. M., D. L. Huber, T. C. Monson, V. Esch, and L. O. Sillerud. 2012. Structural and magnetic characterization of superparamagnetic iron platinum nanoparticle contrast agents for magnetic resonance imaging. *Journal of Vacuum Science & Technology B* 30:1–6.

Xu, Y., Y. Qin, S. Palchoudhury, and Y. Bao. 2011. Water-soluble iron oxide nanoparticles with high stability and selective surface functionality. *Langmuir.* 27:8990–8997.

Yiu, H. H. P., L. Bouffier, P. Boldrin, J. Long, J. B. Claridge, and M. J. Rosseinsky. 2013. comprehensive study of DNA binding on iron(II,III) oxide nanoparticles with a positively charged polyamine three-dimensional coating. *Langmuir.* 29:11354–11365.

Young, A. G., N. Al-Salim, D. P. Green, and A. J. McQuillan. 2008. Attenuated total reflection infrared studies of oleate and trioctylphosphine oxide ligand adsorption and exchange reactions on CdS quantum dot films. *Langmuir.* 24:3841–3849.

Yu, W. W., E. Chang, C. M. Sayes, R. Drezek, and V. L. Colvin. 2006. Aqueous dispersion of monodisperse magnetic iron oxide nanocrystals through phase transfer. *Nanotechnology.* 17: 4483–4487.

Zhao, S-Y., D. K. Lee, C. W. Kim, H. G. Cha, Y. H. Kim, and Y. S. Kang. 2006. Synthesis of Magnetic Nanoparticles of Fe_3O_4 and $CoFe_2O_4$ and Their Surface Modification by Surfactant Adsorption. *Bulletin of the Korean Chemical Society* 27:237–242.

Zhao, Z., Z. Zhou, J. Bao, Z. Wang, J. Hu, X. Chi, et al. 2013. Octapod iron oxide nanoparticles as high-performance T_2 contrast agents for magnetic resonance imaging. *Nature Communications* Article No. 2266.